Geophysical Research Letters

RESEARCH LETTER
10.1029/2025GL115046

Broadband Kinetic Alfvén Waves and the Pitch Angle Distribution of Relativistic Electrons

K. C. Barik[1] and **C. C. Chaston**[1]

[1]Space Sciences Laboratory, University of California, Berkeley, CA, USA

Abstract A statistical survey using 3 years of Van Allen Probes data from 2013 to 2015 is conducted to investigate the impact of broadband kinetic Alfvén waves (KAWs) on the pitch angle distributions (PADs) of relativistic electrons. 62 events exhibiting distinct KAW signatures, identified when other wave modes known to generate butterfly distributions were absent, are examined along with the corresponding PADs of electrons. The results reveal a relationship between the spectral energy density of KAWs and PAD of relativistic electrons, with butterfly PAD features becoming more pronounced and showing larger dip-sizes as the spectral energy density of KAWs increases, particularly for electrons in 0.5–3.4 MeV energy range. At these times the magnetopause sub-solar stand-off distance renders magnetopause shadowing an unlikely formation mechanism. This suggests the interaction of relativistic electrons with broadband KAWs could be a significant mechanism, alongside drift-shell splitting, contributing to the formation of butterfly PADs in the night-side outer radiation belt of Earth.

Plain Language Summary The pitch angle distribution (PAD) of electrons serves as a valuable proxy for understanding the dynamics of Earth's radiation belts, with different distributions linked to distinct physical phenomena. Butterfly pitch angle distributions, characterized by flux minima at 90° and enhanced flux at off-equatorial pitch angles, are typically associated with drift-shell splitting and magnetopause shadowing in the outer radiation belt, as well as acceleration by magnetosonic and chorus waves in the radiation belt. In this study, we present new findings on the relationship between broadband kinetic Alfvén waves (KAWs) and butterfly PADs of relativistic electrons, a connection that has not been explored previously. The simultaneous occurrence of broadband KAWs and butterfly PADs suggests a correlation between the two. Specifically, the spectral energy density of KAWs appears to influence the PAD of energetic electrons, with more pronounced butterfly distributions observed at higher KAW spectral energy densities. This study proposes that broadband KAWs may be a significant factor in modulating butterfly PADs of relativistic electrons, alongside other electromagnetic waves investigated to date.

Key Points:

- The influence of broadband kinetic Alfvén waves (KAWs) on the pitch angle distribution of electrons is investigated
- As the spectral density of KAWs increases, butterfly pitch angle distributions of relativistic electrons become more pronounced
- Interaction of relativistic electrons with KAWs could be another formation mechanism for butterfly distributions in outer radiation belt

Supporting Information:

Supporting Information may be found in the online version of this article.

Correspondence to:

K. C. Barik,
kcbarik@berkeley.edu

Citation:

Barik, K. C., & Chaston, C. C. (2025). Broadband kinetic Alfvén waves and the pitch angle distribution of relativistic electrons. *Geophysical Research Letters*, *52*, e2025GL115046. https://doi.org/10.1029/2025GL115046

Received 23 JAN 2025
Accepted 12 MAY 2025

Author Contributions:

Formal analysis: K. C. Barik
Funding acquisition: C. C. Chaston
Investigation: K. C. Barik
Methodology: K. C. Barik, C. C. Chaston
Project administration: C. C. Chaston
Validation: K. C. Barik, C. C. Chaston
Visualization: K. C. Barik
Writing – original draft: K. C. Barik
Writing – review & editing: K. C. Barik, C. C. Chaston

1. Introduction

Butterfly pitch angle distributions (PADs) are characterized by a depression in particle flux around 90° pitch angle, with enhanced flux at off-equatorial pitch angles (Fritz et al., 2003; Liu et al., 2020; West, 1966; West et al., 1973; Zhao et al., 2014a). Observations suggest that there are two distinct types of butterfly distributions: one with flux maxima at 35 ± 5° and the other at 65 ± 5° (Ni et al., 2016; Ozeke et al., 2022). In time-pitch angle spectrograms, these distributions can take on various shapes, such as bowl-shaped, box-shaped, or a combination of the two (Klida & Fritz, 2009, 2013). Butterfly PADs exhibit strong dependencies on energy, L-shell, and magnetic local time (MLT), showing short-term variations lasting for hours as well as long-term variations over days (Ni et al., 2020; Turner et al., 2012). Butterfly PADs have been observed in various magnetospheric regions, including the dayside magnetosphere, magnetotail, outer radiation belt, inner radiation belt, and slot regions (Klida & Fritz, 2009; Ni et al., 2016; Ozeke et al., 2022; Xiong et al., 2017; Yu et al., 2023; Zhao et al., 2014b). On the nightside, these distributions are predominantly observed at higher L-shells ($\geq 5\ R_E$), while on the dayside, they are more prevalent at lower L-shells (Ni et al., 2016). In the inner radiation belt, butterfly PADs are persistent, whereas in the slot region, their occurrence strongly depends on geomagnetic activity, appearing predominantly during active geomagnetic periods (Zhao et al., 2014b).

Butterfly PADs of electrons can form through various mechanisms. One significant factor is asymmetries in the geomagnetic field that cause pitch-angle dependent adiabatic distortions of energetic electron drift paths via drift shell splitting (Schulz & Lanzerotti, 1974). These magnetic asymmetries may be in the form of day-night

distortions of geomagnetic field arising from the interaction between the magnetosphere and solar wind (Roederer, 1967), substorm driven magnetic distortions due to local plasma injections (Xiong et al., 2017) or due to contracting dipolarization fronts during geomagnetic storms (Yu et al., 2023) among other possible scenarios. If the magnetopause is compressed during geomagnetically active conditions, electrons at large pitch-angles can be lost to interplanetary space, leading to the formation of magnetospheric butterfly PADs (Fritz et al., 2003; Klida & Fritz, 2009, 2013; Roederer, 1967; Roederer & Schulz, 1969, 1971; Xiang et al., 2018; Xiao et al., 2015). However, for sufficiently large radial gradients in phase space density butterfly PADs in the distorted geomagnetic field may be formed due to the action of drift shell splitting alone (Selesnick & Blake, 2002).

More recently, non-adiabatic processes involving small scale distortions of the geomagnetic field (Artemyev et al., 2015) and interactions with whistler and magnetosonic waves have been suggested as formation mechanisms for butterfly PADS (Haas et al., 2023; Horne et al., 2005; Li et al., 2016; Ni et al., 2020; Xiao et al., 2015). These mechanisms may account for the occurrence of butterfly PADs deep inside the inner magnetosphere and during geomagnetically quiet conditions when drift shell splitting may be suppressed. On the other hand, the prevalence of butterfly PADs through pre-midnight to dawn ($\sim 20 - 04\ MLT$) sector (Ni et al., 2016; Ozeke et al., 2022) aligns well with kinetic Alfvén waves (KAWs) (Chaston et al., 2015), suggesting a potential link between these phenomena. This association is supported by numerical models for diffusion in Alfvénic turbulence (Chaston, 2023), which indicate that KAWs drive significant pitch-angle dependent diffusion both across L-shells and through pitch-angle. These considerations warrant further investigation to better understand the relationship between KAWs and butterfly PADs from direct observation.

In this study, we analyze 3 years of Van Allen Probes (VAPs) data, spanning 2013–2015, identifying intervals where KAWs are observed when no other wave modes known to drive butterfly PADs are present, to investigate the relationship between these waves and the PADs of energetic electrons in the outer radiation belt. This paper is organized as follows: The data sets and event selection criteria are described in Section 2. A case study example is presented in Section 3. The results of the statistical investigation are provided in Section 4. A discussion of the findings relative to drift shell splitting and KAW scattering is then given in Section 5, followed by the conclusions in Section 6.

2. Event Selection

KAW events are identified by eye from an examination of VAPs survey mode electromagnetic field measurements provided by the EMFISIS (Kletzing et al., 2013) and EFW instruments (Wygant et al., 2013) over the years 2013–2015, in which broadband electromagnetic fluctuations with decreasing spectral energy density over the range from $\sim 0.1 - 10$ Hz (ULF-ELF range) were present but band-limited and higher frequency emissions (e.g., chorus, EMICWs and magnetosonic waves) at frequencies extending up to 10 kHz were absent. The duration of each event was defined by the length of the interval over which the broadband ELF fluctuations were observed. This approximately corresponds to a threshold of $\sim 10^{-4}\ (mV/m)^2/Hz$ at 10 Hz in the electric field component returned by the EFW survey plots (https://rbsp.space.umn.edu/survey/—see Figure S1 in Supporting Information S1) and $10^{-1}\ (mV/m)^2/Hz$ and $10^{-2}\ nT^2/Hz$ at 0.1 Hz from the FFT of the spin plane time series data in **E** and flux-gate magnetometer (FGM) **B** as shown in Figures 1b and 1c. For electron pitch angles with energies ranging from 50 keV to 1 MeV, data from the Magnetic Electron Ion Spectrometer (MagEIS), which provides measurements at 11 pitch angle intervals, are used (Blake et al., 2013). For higher-energy electrons, ranging from 1 to 20 MeV, measurements from the Relativistic Electron Proton Telescope (REPT), with data provided at 17 pitch angle intervals, are included (Baker et al., 2012). Additionally, solar wind parameters with a 1-min time resolution are obtained from the OMNI database (NASA/GSFC, OMNIWeb, https://omniweb.gsfc.nasa.gov/). Only events where signatures of KAWs were present and those wave modes that have previously been identified as drivers of butterfly distributions were absent, are included in the statistical analysis. This approach allows us to isolate and study the specific effects of broadband KAWs on the PADs of radiation belt electrons. Please note that the selection of these events is independent of the energetic electron measurements.

3. Case Study KAW Example

Figure 1 presents a representative KAW event recorded on 6 May 2013, from 07:00 to 11:00 UT, during which VAPs A traveled from L-shell 5–6. A broadband spectrum as a function of spacecraft (SC) frame frequency (f_{sc}) is observed in the X_{MGSE} and Y_{MGSE} components of the magnetic and electric fields, respectively, as shown in

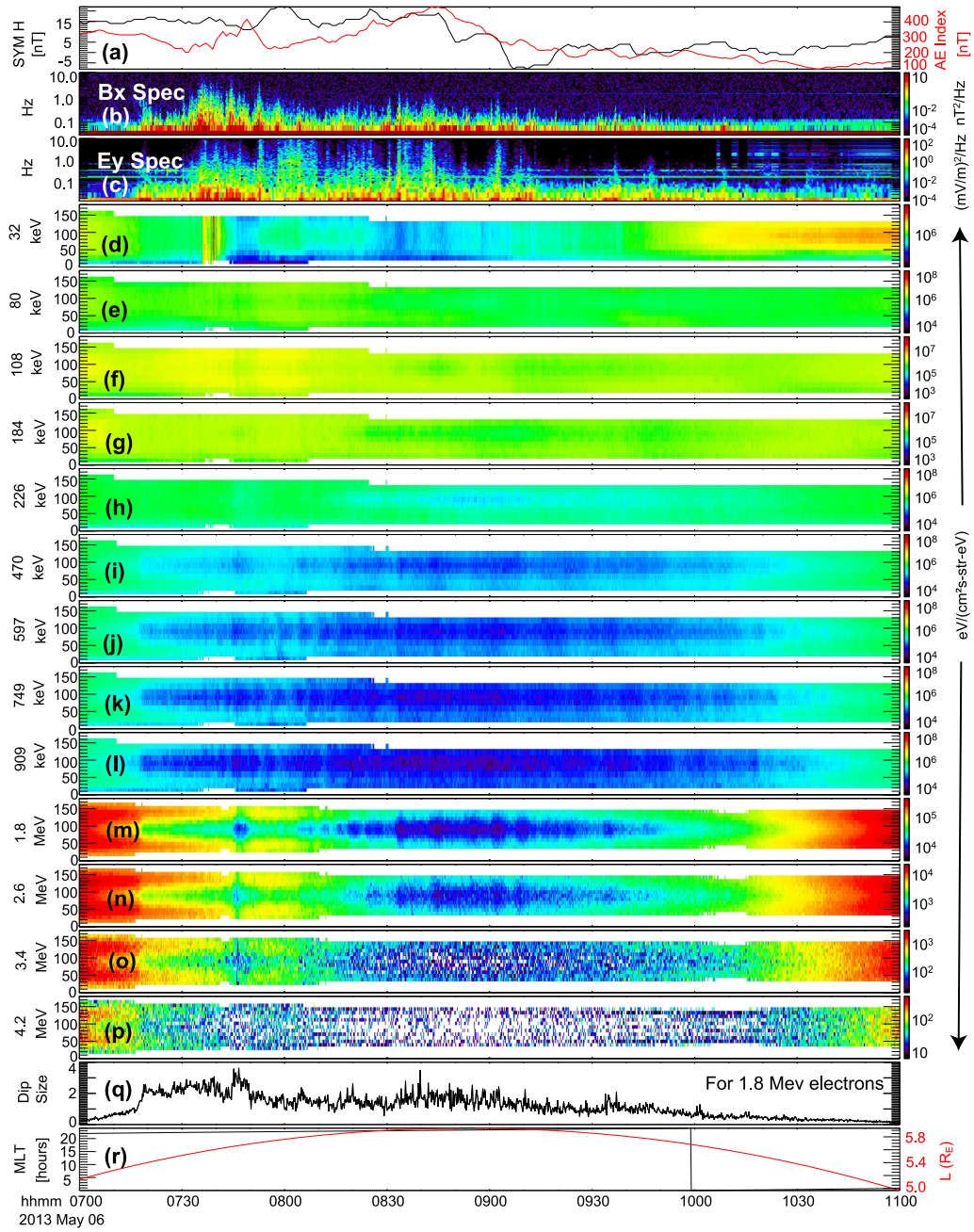

Figure 1. Kinetic Alfvén wave event from RBSP A when traveling from L-shell 5–6 on 6 May 2013 from 07:00 to 11:00 UT. Panel (a) SYM H and Auroral Electrojet indices. Spectrogram of (b) *x*-component of magnetic field and (c) *z*-component of electric field in MGSE-coordinates. Pitch angle distribution of electrons with energies (d) 32, (e) 80, (f) 108, (g) 184, (h) 226, (i) 470, (j) 597, (k) 749, (l) 909 keV, (m) 1.8, (n) 2.6, (o) 3.4, and (p) 4.2 MeV. Panel (q) represents the dip size plotted against time for the 1.8 MeV energy channel. Finally, magnetic local time (hours) and L-shell (in R_E) is plotted in panel (r).

Figures 1b and 1c. Here X_{MGSE} aligns with the SC spin axis, which is approximately Sun directed. The Y_{MGSE} and Z_{MGSE} lie within the SC spin plane, oriented roughly along the Y and Z-GSE directions (Russell, 1971). These broadband features often occur following injections of energized plasma, as indicated by the Auroral Electrojet (AE) index, even though the SYM-H index reflects quiet conditions (Figure 1a), reaching barely −5 nT. Notably, the wave energy density decreases with increasing wave frequency, and the wave signatures extend to higher frequencies in the electric field compared to the magnetic field. Figures 1c–1p display color-coded differential fluxes of electrons as a function of pitch angle and time, with electron energies ranging from 33 keV to 4.2 MeV,

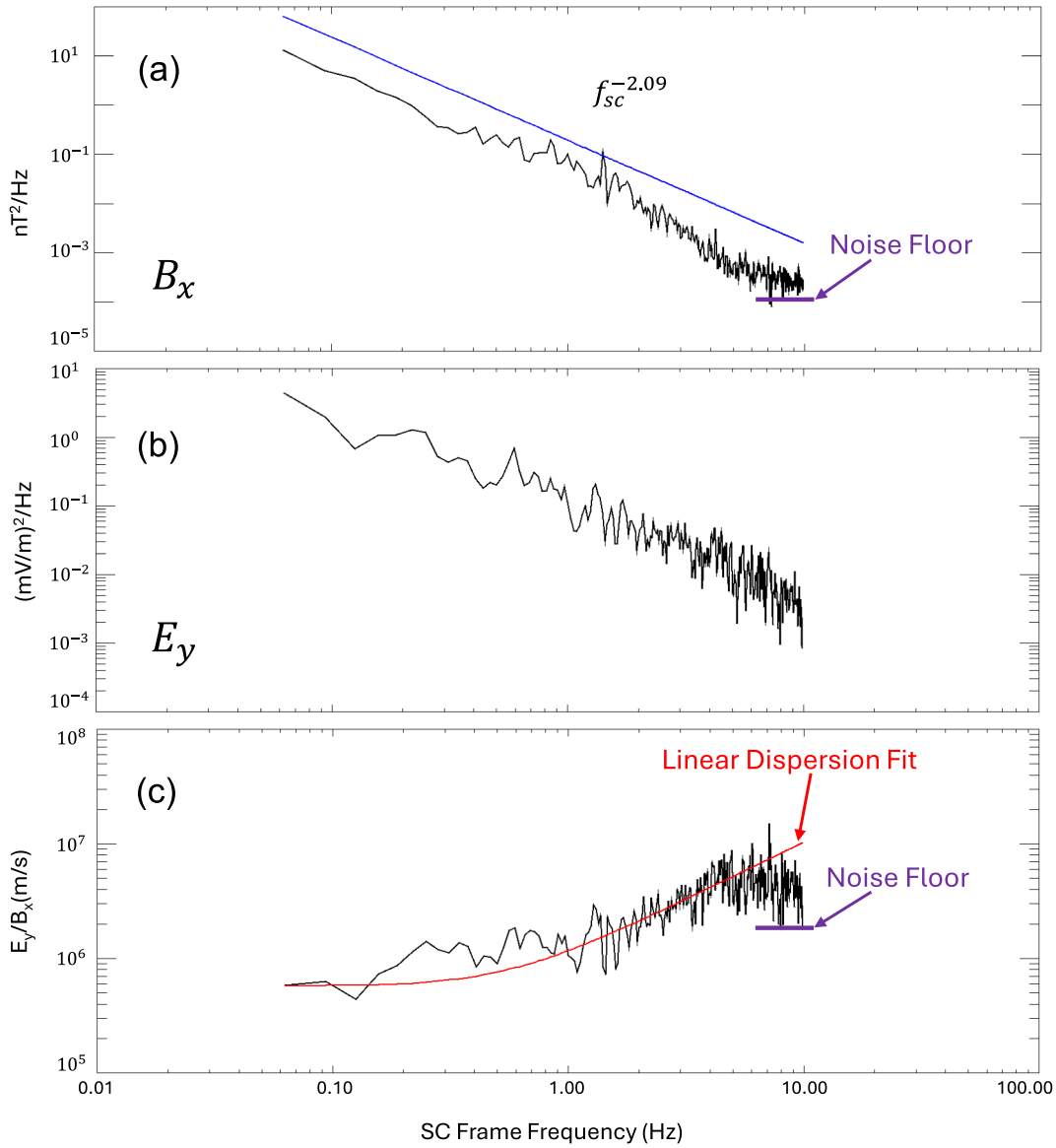

Figure 2. Shows (a) magnetic spectral energy density (black curve) fitted with a power law (blue line), (b) electric field spectral energy density, and (c) the ratio of E_y/B_x (black curve) fitted with the linear impedance relation of kinetic Alfvén waves (red curve). Appearance of noise floor is marked in purple.

as indicated on the respective panels. These measurements are obtained from the MagEIS and REPT instruments onboard VAPs. The data reveal that lower-energy electrons exhibit a pancake distribution (having peak flux around 90°). As the electron energy increases, the distribution transitions to a butterfly distribution, first appearing at an energy of 226 keV. The butterfly PADs becomes increasingly pronounced with electron energies up to 2.6 MeV. Beyond this energy, the butterfly distribution begins to distort and eventually disappears at higher electron energies. The difference in electron flux, hereafter referred to as the dip size [DS $= (Max\ Flux - Flux_{at\ 90^\circ})/Flux_{at\ 90^\circ}$], is plotted as a function of time for the 1.8 MeV energy channel in Figure 1q. The plot reveals that the DS closely follows the evolution of the spectral energy density shown in Figures 1b and 1c. Figure 1r shows the corresponding MLT and L-shell values during the event.

To facilitate mode identification of the fluctuations shown in Figures 1b and 1c, the averaged spectrum in these fields are evaluated as presented in Figures 2a and 2b as a function of f_{sc}. It can be seen that both the electric and magnetic field components follow similar trends. A fit to the magnetic field spectra (ϵ_b) returns a power law

varying as $\epsilon_b \propto f_{sc}^{-2.09}$, as shown in Figure 2a in blue. This result is in agreement with the statistical results from Chaston et al. (2015) over a similar frequency range. Additionally, the spectral energy density ratio (E_y/B_x) is fitted with the linear impedance relation for KAWs as described by (Barik et al., 2019, 2024; Chaston et al., 2015; Lysak & Lotko, 1996; Stasiewicz et al., 2000)

$$\frac{E_y}{B_x} \approx \frac{B_0}{\sqrt{\mu_0 m_i n_i}} \sqrt{1 + (\omega_{sc}/\Omega_i)^2 \left(\frac{V_i}{V_f}\right)^2}. \quad (1)$$

Here, B_0 represents the total ambient magnetic field and μ_0 denotes the permeability of free space. ω_{sc} is the measured wave frequency in the spacecraft frame, while $\Omega_i = \left(\frac{q_i B_0}{m_i}\right)$ represents the angular ion cyclotron frequency, with q_i and m_i denoting the charge, and mass of ions, respectively. Furthermore, V_i, and V_f represent ion thermal speed and flow speed in the spacecraft frame, respectively. We set n_i and V_i/V_f to be the free parameters with $V_A = B_0/\sqrt{\mu_0 m_i n_i}$ the Alfvén speed. It is worth noting that the finite electron temperature is not included in the KAW impedance relation used here because in this environment $T_i > T_e$. Following the studies by Chaston et al. (2012, 2014) and Malaspina et al. (2015), since $k_\perp \gg k_\parallel$ for KAWs, we can approximate $k \approx k_\perp$ which implies $V_A \gg \omega/k$ with $\omega \ll \Omega_i$ the wave frequency in the plasma frame. For oscillations on scales of the order of thermal ion gyro-radii and less, and flow speeds during events of this type, ω_{sc} is dominated by $k_\perp V_f$ allowing the magnitude of $k_\perp$ to be estimated as ω_{sc}/V_f in Equation 1. In Figure 2c, the black curve represents the observed impedance spectrum, while the red curve shows the fit of Equation 1 demonstrating consistency with the interpretation of the wave fields as a Doppler-shifted spectrum of broadband KAWs up to $f_{sc} \approx 5 - 6Hz$. The fit provides $n_i \approx 2.0\ cm^{-3}$ and $\frac{V_i}{V_f} = 4.0$ in agreement with earlier results (Chaston et al., 2014), in the same general plasma environment. Beyond 5–6 Hz in f_{sc} the digitization noise floor of the FGM measurement is encountered (Kletzing et al., 2013) and the impedance measurement rendered invalid. This floor is marked with purple color line in Figures 2a and 2c.

4. KAW Statistics and Butterfly PADs

Over the period from 2013 to 2015 we have identified 62 similar events from VAPs A. This is the subset of KAW events reported over this interval (Chaston et al., 2015) in which those wave modes in the outer radiation belt that classically drive the modification of energetic electron PADs (Blum & Breneman, 2020) are absent. Figure 3a shows the central location of each event in our survey in MLT and L-shell. While each event is represented here by a single point it should be noted that these events often persist for hours along VAPs trajectories outside the plasmapause, corresponding to more than an hour in local time on this plot. Most events are distributed over L-shell 5–6.5 within the outer radiation belt and are located over MLT 19–02, with predominant occurrence in the pre-midnight sector. This subset replicates similar MLT and L-shell distributions reported by Chaston et al. (2015).

As represented in Figure 2a, a key characteristic of KAW spectra are magnetic spectral energy densities that follow power laws formulated as $\epsilon_b = A f_{sc}^{-\alpha}$. The consistency of this form allows the whole spectrum to be characterized by measurements of ϵ_b at a single f_{sc} for a known value of α (Chaston et al., 2015). We exploit this characteristic here to quantify the spectral energy density present in KAWs in each event in our survey by measuring ϵ_b at those f_{sc} corresponding to $k_\perp \rho_i = 1$, noting that $\alpha \approx 2$ across all events. The translation from f_{sc} to $k_\perp \rho_i$ is performed using fits of Equation 1 to the observed impedance ratio in the manner performed in Figure 2c and more broadly in Chaston et al. (2015). This results in a database of single valued spectral energy densities representative of each wave event that can be compared to variations in the coincident particle distributions within each event and across the database.

To perform these comparisons, we average the differential energy flux measured from the REPT and MagEIS instruments in each energy bin as a function of pitch-angle over each event. In performing this reduction, the REPT data is down-sampled in pitch-angle to match the resolution of the MagEIS fluxes. These average PADs are then sorted into bins defined by the spectral energy density range of four logarithmically spaced levels of KAW activity. The range of these bins is selected to provide sufficient statistics in each bin and can be related to AE and Dst via the empirical relationships defined in Chaston et al. (2015) and to SYM-H in Figure 4b to be discussed in

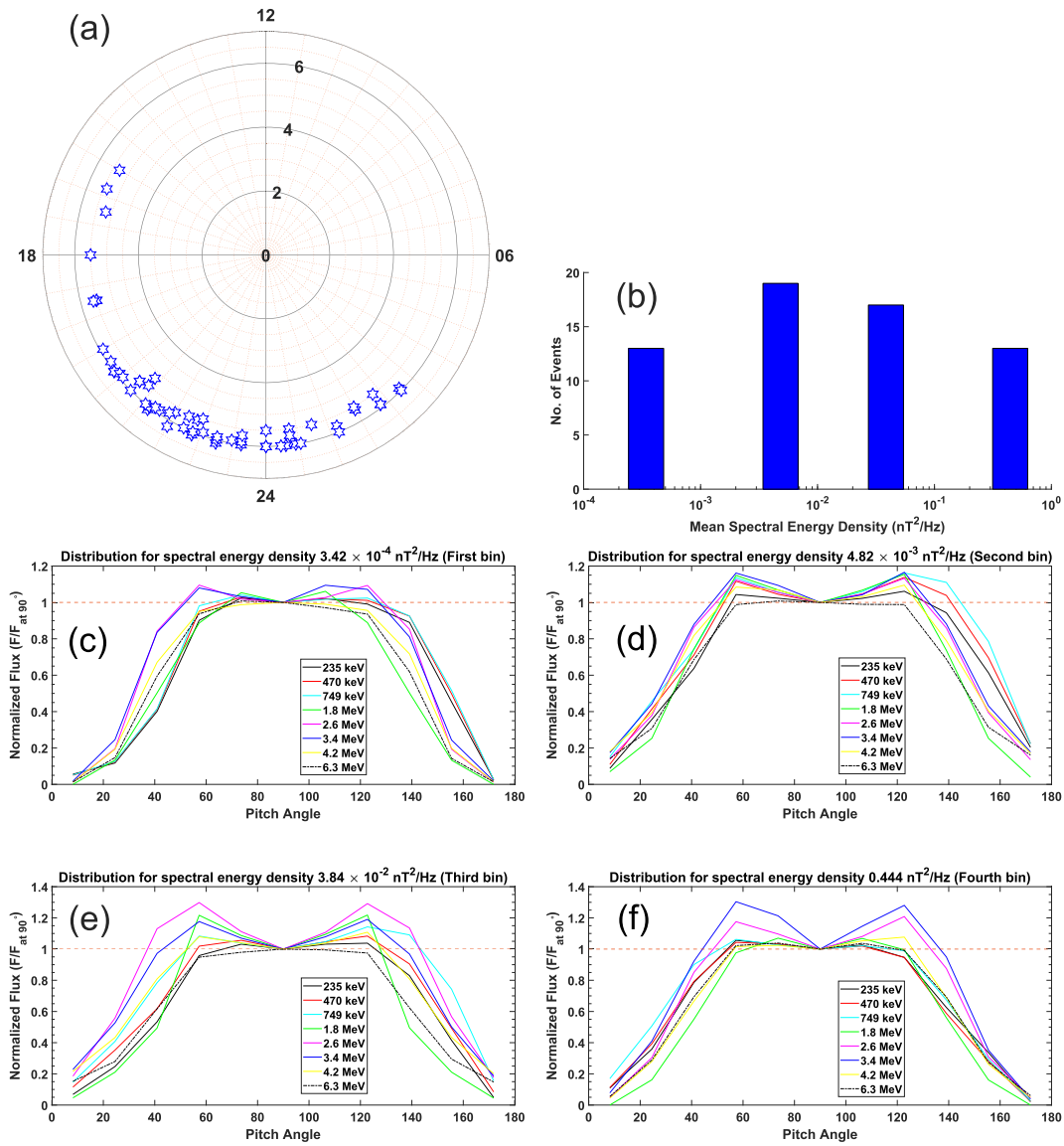

Figure 3. Shows (a) occurrence of the events as a function of magnetic local time and L-shell and (b) bar plot showing the distribution of number of events for each spectral energy density bin. The distribution of electron flux (normalized to the minimum flux at 90°) against the pitch angle for four spectral energy density bins of kinetic Alfvén waves having mean value as (c) 3.42 $\times$ 10^{-4} nT^2/Hz, (d) 4.82 $\times$ 10^{-3} nT^2/Hz, (e) 3.84 $\times$ 10^{-2} nT^2/Hz, and (f) 0.444 nT^2/Hz, respectively. The horizontal red dashed line at a normalized flux value of 1 serves as the baseline for identifying the butterfly pitch angle distributions.

the next section. Note that no time averaging occurs during this process, so no event is emphasized more than the other. Figure 3b shows the histogram of events in each of these bins and the central magnetic spectral energy of each. The corresponding averaged PADs are presented in Figures 3c–3f over the range 0° to 180° for each wave spectral energy bin. To avoid overcrowding, not all energy channels are shown. Note that the PADs corresponding to energy channels 356, 595 keV, and 2.1 MeV not shown here, follow the similar pattern. These fluxes are normalized by that at 90° with the title of each panel specifying the corresponding KAW central spectral energy density. A horizontal red dashed line at a normalized flux value of 1 acts as a reference, aiding in the identification of butterfly distributions. Distributions providing double peak flux maxima roughly symmetric about 90° and above this reference line are classified as butterfly distributions.

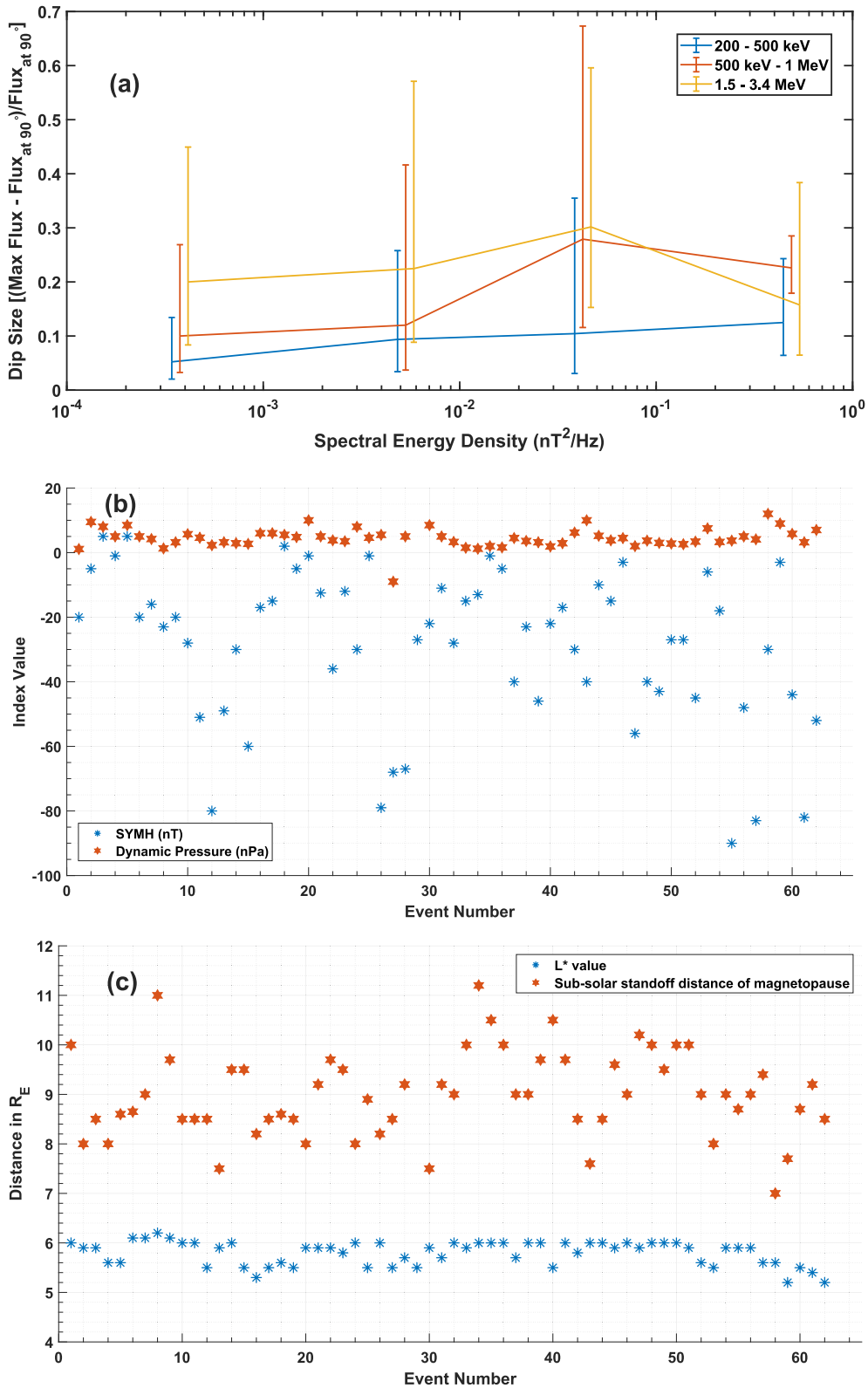

Figure 4. Shows (a) the variation of dip size (DS) with spectral energy density for different electron energy ranges, the standard deviation is plotted as error bars. A detailed figure illustrating the distribution of DS across each spectral energy density bin is provided in Figure S2 in Supporting Information S1. Variation of (b) SYM H index and the solar-wind dynamic pressure for event number mentioned on abscissa and (c) the sub-solar stand-off distance and the event location L* value in R_E corresponding to these events.

Inspection of these panels indicates that as the KAW spectral energy density increases, there is a tendency toward the formation and intensification of butterfly distributions. Notably, some energy ranges initially lacking a butterfly distribution at lower spectral densities begin to display this form at higher spectral densities. For example, PADs of electrons with energies from 235 keV to 3.4 MeV show a butterfly distribution at the first spectral energy density bin of $3.42 \times 10^{-4}\ nT^2/Hz$, whereas higher-energy electrons do not exhibit this pattern. When the KAW spectral energy density rises by an order of magnitude in the second bin (i.e., $4.82 \times 10^{-3}\ nT^2/Hz$), 4.2 MeV electrons begin to display a butterfly distribution. Higher-energy electrons require even larger spectral densities to develop butterfly PADs. In this study, the PADs of 6.3 MeV electrons only show butterfly distributions at the fourth bin, with a KAW spectral energy density of $0.444\ nT^2/Hz$. These observations suggest that higher spectral energy densities of KAWs are necessary for the highest energy electrons sampled to exhibit butterfly characteristics in their PADs.

To further investigate the dependency of electron PAD driven by KAWs, Figure 4a presents the normalized statistical variation of the difference between the differential electron flux on the "wings" of the observed butterfly PADS to that measured at a pitch-angle of 90° as a function of spectral energy at $k_\perp \rho_i = 1$. The spectral energy density bins are the same as those used in the preparation of Figure 3. The 3 curves shown correspond to log-normal averages performed over energy ranges we label as "energetic" (blue, 200–500 keV), "relativistic" (red, 0.5–1.0 MeV), and "ultra-relativistic" (orange, 1.8–3.4 MeV) roughly following the classification of Drozdov et al. (2015) and Usanova et al. (2014). Note that the DS is computed for each event separately, and the statistics are based on the distribution of these values across all events in the corresponding energy categories. As a result, the representation of the DS is based on the statistical distribution of events, not the time-averaged data. Since each event in the data set has its own duration, the statistical analysis is based on the number of events in each energy range, rather than the length of individual events, thereby excludes time averaging. The error bars represent the standard deviation of the log-normal distribution describing the distribution of DS values in each bin. To enhance clarity, successive energy curves are offset by a factor of 1.1 in spectral energy density.

Inherent to the dependencies presented in Figure 4a is uncertainty in the time history of interaction along drift orbits through the inhomogeneous geomagnetic field. We shall address the consequences of the distorted field in the subsequent section, but acknowledge here that these considerations mean that a simple monotonic relationship between DS and spectral energy is not necessarily expected. Nonetheless, dependencies do emerge in these trends consistent with the action of KAWs. First, the DS generally increases with energy across all spectral density energy bins. This is an expected consequence of the action of KAWs for which pitch-angle diffusion coefficients increase with energy through the observed range (Chaston, 2023). As per the numerical model (Chaston, 2023), the diffusive time scale of MeV electrons is as short as 100 s, while the wave lasts up to hours. Consequently, electrons that spend tens of seconds per MLT hour can undergo multiple drift orbits and repeatedly interact with KAWs. Second, with the exception of those distributions compiled during the strongest KAW events, there is a general increase in DS with spectral energy density that is manifested through both the log-normal averages in each spectral energy bin and the width of the DS distributions represented here by the error bars. Given the uncertainty in the time-history the latter is perhaps the stronger indicator of the action of KAWs. The apparent aberration in this trend for the largest spectral energy densities may be a consequence of reduced statistics in the higher energy ranges for large ϵ_b and reduced interaction times since the largest spectral energy densities are generally recorded in the early phases of a geomagnetic storm or general disturbance of the magnetosphere (Chaston et al., 2015).

5. Drift Shell Splitting and KAW Scattering

The KAW events and coincident electron distributions considered in this statistical analysis are observed in the absence of those modes shown previously to promote the formation of butterfly distributions (Blum & Breneman, 2020; Haas et al., 2023; Horne et al., 2005; Li et al., 2016; Ni et al., 2020; Xiao et al., 2015). While we cannot exclude the occurrence of these modes along an entire electron drift path their absence in our survey renders the case for their involvement perhaps less compelling than that of the KAWs which are observed over extended regions in local time and L-shell through the events considered. On the other hand, since the majority of selected wave events occur during intervals of enhanced geomagnetic activity, distortions of Earth's dipolar field can be expected to provide pitch-angle dependent drift paths that drive the formation of butterfly PADs on gradients in

phase space density across L-shells and/or via losses at large pitch-angle through a compressed magnetopause (magnetopause shadowing) (Smirnov et al., 2022; Turner et al., 2019; Zhao et al., 2018).

To illustrate the connection between these events and geomagnetic activity, Figure 4b shows the variation in SYM-H values (blue asterisks) and the solar-wind dynamic pressure (red stars) across the event sequence. The plot shows that a significant proportion of events align with periods of active geomagnetic conditions. To assess whether the observed butterfly PADs in these events may result from magnetopause shadowing, the sub-solar standoff distance of the magnetopause during each wave event is estimated using Shue's model (Shue et al., 1997, 1998), which is expressed as follows:

$$r_0 = \{10.22 + 1.29\,tanh[0.184(B_z + 8.14)]\}(D_p)^{-\frac{1}{6.6}}. \quad (2)$$

The parameters B_z and D_p in Equation 2 represent the z-component of the interplanetary magnetic field $(IMF\ B_z)$ and the solar wind dynamic pressure, respectively. The 1 min time resolution data for the periods of the events were obtained from the OMNI database, and subsequently smoothed by a 5 min running average window for the analysis. The results of this analysis are presented in Figure 4c. The sub-solar standoff distance of the magnetopause, calculated using Equation 2, is marked by red stars in Figure 4c, while the locations of the wave events (L* values) are indicated by blue asterisks and both are plotted against event's number. The figure shows that, in most cases, the magnetopause is located well beyond 8 R_E of Earth's surface, whereas the KAW associated butterfly PAD events consistently occur within $L^* = 6\ R_E$. Given the correspondingly large displacement between the location of PAD observation and the magnetopause we suggest that it is unlikely that the butterfly distributions observed in our survey are a consequence losses through the magnetopause except in the most extreme cases.

While pitch-angle scattering in alternate wave modes and magnetopause shadowing may be less likely formation mechanisms for the butterfly PADs reported here, drift-shell splitting on negative phase space density gradients that exist over the L-shell range of our survey may be expected to form PADs similar to those we report (Selesnick & Blake, 2002; Turner et al., 2019). Our observations however suggest that this may not be the only mechanism active in forming these PADS. We note that every KAW event in our survey is coincident with MeV butterfly PADs and that the observed wave-fields extend over a significant fraction of a drift orbit. It may be expected then that a scattering process is also active in forming these distributions because it has been demonstrated that KAWs act to violate the invariants that govern the formation of butterfly PADs via the shell splitting process (Chaston, 2023; Chaston et al., 2018). While a quantitative demonstration goes beyond what can be achieved here the timescales for radial diffusion for observed KAW wave spectra on these L-shells is less than the drift period at radiation belt energies of 0.5–3.4 MeV and peaked at intermediate pitch angles. Much like drift shell splitting, the consequent transport can be expected to modulate PADs dependent on the radial gradients in phase density. On the other hand, pitch-angle diffusion coefficients in these waves through the outer radiation belt maximize at 90° with strong gradients in these coefficients with decreasing pitch-angle. The wave particle interaction is the dominant process leading to depletion at 90°. While pitch-angle scattering is the main cause of the formation of butterfly distributions and depletion at 90°, the specific form is modulated by wave driven radial transport which may serve to enhance or reduce the effect depending on the local gradients in phase space density and the direction of transport (Chaston, 2025).

This assertion is supported by the survey of Ozeke et al. (2022) that distinguishes between butterfly PADs caused by wave-particle interactions and those associated with magnetopause shadowing. These authors assert that PADs with maxima at 65 ± 5° are driven by wave-particle interactions, whereas those with maxima at lower pitch angles are linked to magnetopause shadowing. In our study, the former feature is consistently observed across all analyzed events. This findings together with those described above suggest that the butterfly PADs reported in our survey may be a consequence of the combined action of scattering in KAWs over those portions of drift orbits that are immersed in KAWs and drift-shell splitting over those portions of these orbits where KAWs are absent.

6. Conclusion

A statistical analysis of VAPs-A data from 2013 to 2015, encompassing 62 events of broadband KAWs, was conducted to investigate their relationship with electron PADs. The findings reveal that KAWs may influence electron PADs. Notably, KAWs appear to exert the most persistent and pronounced effect on relativistic and ultra-

relativistic electrons in the 0.5–3.4 MeV range, where butterfly distributions become increasingly prominent. These distributions in general show enhanced average DS and variation in DS with increasing KAW spectral energy density. Estimates of the magnetopause location for observed upstream parameters through this survey confirm that magnetopause shadowing is unlikely to account for the butterfly form of the PADs observed. Since it is not possible to disentangle the range of competing interactions that define the energetic electron distributions from single point, or even two point measurements from the VAPs, confirmation of a physical connection between KAWs and butterfly PADs of radiation belt electrons requires global simulations that may be compared to the results from this statistical study.

Data Availability Statement

The data sets used in this study are publicly available at the following data repositories: EMFISIS https://emfisis.physics.uiowa.edu/Flight/, EFW https://www.space.umn.edu/rbspefw-data/, HOPE/MAGEIS/REPT https://cdaweb.gsfc.nasa.gov/pub/data/rbsp/rbspa/l2/ect/, and OMNI https://omniweb.gsfc.nasa.gov/. The data analyses were performed using publicly available IDL based SPEDAS software (Angelopoulos et al., 2019) available at http://spedas.org/wiki/index.php?title=Downloads_and_Installation. The high level data sets used to generate the figures are available at Barik and Chaston (2025).

Acknowledgments
This research was supported by the NSF Award 2041971.

References

Angelopoulos, V., Cruce, P., Drozdov, A., Grimes, E. W., Hatzigeorgiu, N., King, D. A., et al. (2019). The space physics environment data analysis system (SPEDAS). *Space Science Reviews*, *215*(1), 9. https://doi.org/10.1007/s11214-018-0576-4

Artemyev, A. V., Agapitov, O. V., Mozer, F. S., & Spence, H. (2015). Butterfly pitch angle distribution of relativistic electrons in the outer radiation belt: Evidence of nonadiabatic scattering. *Journal of Geophysical Research: Space Physics*, *120*(6), 4279–4297. https://doi.org/10.1002/2014JA020865

Baker, D. N., Kanekal, S. G., Hoxie, V. C., Batiste, S., Bolton, M., Li, X., et al. (2012). The relativistic electron-proton telescope (REPT) instrument on board the radiation belt storm probes (RBSP) spacecraft: Characterization of Earth's radiation belt high-energy particle populations. *Space Science Reviews*, *179*(1–4), 337–381. https://doi.org/10.1007/s11214-012-9950-9

Barik, K. C., & Chaston, C. C. (2025). Broadband kinetic Alfvén waves and the pitch angle distribution of relativistic electrons. https://doi.org/10.6084/m9.figshare.28260164

Barik, K. C., Singh, S. V., & Lakhina, G. S. (2019). Resonant instabilities of kinetic Alfvén waves in the Earth's magnetosphere with superthermal electrons. *Physics of Plasmas*, *26*(11), 112108. https://doi.org/10.1063/1.5114907

Barik, K. C., Singh, S. V., & Lakhina, G. S. (2024). A comparative study of ion beam and velocity shear driven resonant instability of kinetic Alfvén waves with κ-electrons. *Advances in Space Research*, *73*(12), 6041–6053. https://doi.org/10.1016/j.asr.2024.03.034

Blake, J. B., Carranza, P. A., Claudepierre, S. G., Clemmons, J. H., Crain, W. R., Dotan, Y., et al. (2013). The magnetic electron ion spectrometer (MAGEIS) instruments aboard the radiation belt storm probes (RBSP) spacecraft. *Space Science Reviews*, *179*(1–4), 383–421. https://doi.org/10.1007/s11214-013-9991-8

Blum, L. W., & Breneman, A. W. (2020). Observations of radiation belt losses due to cyclotron wave-particle interactions (pp. 49–98). https://doi.org/10.1016/B978-0-12-813371-2.00003-2

Chaston, C. C. (2023). Electron scattering, transport and energization by Alfvénic turbulence in Earth's outer radiation belt. *Geophysical Research Letters*, *50*(13), e2023GL104243. https://doi.org/10.1029/2023GL104243

Chaston, C. C. (2025). Driving Earth's outer radiation belt with Alfvénic turbulence. *Geophysical Research Letters*, *52*(8), e2025GL115125. https://doi.org/10.1029/2025GL115125

Chaston, C. C., Bonnell, J. W., Clausen, L., & Angelopoulos, V. (2012). Correction to "energy transport by kinetic-scale electromagnetic waves in fast plasma sheet flows". *Journal of Geophysical Research*, *117*(A12). https://doi.org/10.1029/2012JA018476

Chaston, C. C., Bonnell, J. W., Kletzing, C. A., Hospodarsky, G. B., Wygant, J. R., & Smith, C. W. (2015). Broadband low-frequency electromagnetic waves in the inner magnetosphere. *Journal of Geophysical Research: Space Physics*, *120*(10), 8603–8615. https://doi.org/10.1002/2015JA021690

Chaston, C. C., Bonnell, J. W., Wygant, J. R., Mozer, F., Bale, S. D., Kersten, K., et al. (2014). Observations of kinetic scale field line resonances. *Geophysical Research Letters*, *41*(2), 209–215. https://doi.org/10.1002/2013GL058507

Chaston, C. C., Bonnell, J. W., Wygant, J. R., Reeves, G. D., Baker, D. N., & Melrose, D. B. (2018). Radiation belt "dropouts" and drift-bounce resonances in broadband electromagnetic waves. *Geophysical Research Letters*, *45*(5), 2128–2137. https://doi.org/10.1002/2017GL076362

Drozdov, A. Y., Shprits, Y. Y., Orlova, K. G., Kellerman, A. C., Subbotin, D. A., Baker, D. N., et al. (2015). Energetic, relativistic, and ultra-relativistic electrons: Comparison of long-term verb code simulations with Van Allen probes measurements. *Journal of Geophysical Research: Space Physics*, *120*(5), 3574–3587. https://doi.org/10.1002/2014JA020637

Fritz, T. A., Alothman, M. J., Bhattacharjya, J., Matthews, D. L., & Chen, J. (2003). Butterfly pitch-angle distributions observed by ISEE-1. *Planetary and Space Science*, *51*(3), 205–219. https://doi.org/10.1016/s0032-0633(02)00202-7

Haas, B., Shprits, Y. Y., Allison, H. J., Wutzig, M., & Wang, D. (2023). A missing dusk-side loss process in the terrestrial electron ring current. *Scientific Reports*, *13*(1), 970. https://doi.org/10.1038/s41598-023-28093-2

Horne, R. B., Thorne, R. M., Glauert, S. A., Albert, J. M., Meredith, N. P., & Anderson, R. R. (2005). Timescale for radiation belt electron acceleration by whistler mode chorus waves. *Journal of Geophysical Research*, *110*(A3), A03225. https://doi.org/10.1029/2004JA010811

Kletzing, C. A., Kurth, W. S., Acuna, M., MacDowall, R. J., Torbert, R. B., Averkamp, T., et al. (2013). The electric and magnetic field instrument suite and integrated science (EMFISIS) on RBSP. *Space Science Reviews*, *179*(1–4), 127–181. https://doi.org/10.1007/s11214-013-9993-6

Klida, M. M., & Fritz, T. A. (2009). The Earth's magnetopause as a source and sink for equatorial nightside energetic charged particles. *Annales Geophysicae*, *27*(11), 4305–4316. https://doi.org/10.5194/angeo-27-4305-2009

Klida, M. M., & Fritz, T. A. (2013). Characterising electron butterfly pitch angle distributions in the magnetosphere through observations and simulations. *Annales Geophysicae*, *31*(2), 305–314. https://doi.org/10.5194/angeo-31-305-2013

Li, J., Ni, B., Ma, Q., Xie, L., Pu, Z., Fu, S., et al. (2016). Formation of energetic electron butterfly distributions by magnetosonic waves via Landau resonance. *Geophysical Research Letters*, *43*(7), 3009–3016. https://doi.org/10.1002/2016GL067853

Liu, C. M., Fu, H. S., Liu, Y. Y., Wang, Z., Chen, G., Xu, Y., & Chen, Z. Z. (2020). Electron pitch-angle distribution in Earth's magnetotail: Pancake, cigar, isotropy, butterfly, and rolling-pin. *Journal of Geophysical Research: Space Physics*, *125*(4), e2020JA027777. https://doi.org/10.1029/2020JA027777

Lysak, R. L., & Lotko, W. (1996). On the kinetic dispersion relation for shear Alfvén waves. *Journal of Geophysical Research*, *101*(A3), 5085–5094. https://doi.org/10.1029/95JA03712

Malaspina, D. M., Claudepierre, S. G., Takahashi, K., Jaynes, A. N., Elkington, S. R., Ergun, R. E., et al. (2015). Kinetic Alfvén waves and particle response associated with a shock-induced, global ULF perturbation of the terrestrial magnetosphere. *Geophysical Research Letters*, *42*(21), 9203–9212. https://doi.org/10.1002/2015GL065935

Ni, B., Yan, L., Fu, S., Gu, X., Cao, X., Xiang, Z., & Zhang, Y. (2020). Distinct formation and evolution characteristics of outer radiation belt electron butterfly pitch angle distributions observed by Van Allen probes. *Geophysical Research Letters*, *47*(4), e2019GL086487. https://doi.org/10.1029/2019GL086487

Ni, B., Zou, Z., Li, X., Bortnik, J., Xie, L., & Gu, X. (2016). Occurrence characteristics of outer zone relativistic electron butterfly distribution: A survey of Van Allen probes REPT measurements. *Geophysical Research Letters*, *43*(11), 5644–5652. https://doi.org/10.1002/2016GL069350

Ozeke, L. G., Mann, I. R., Olifer, L., Claudepierre, S. G., Spence, H. E., & Baker, D. N. (2022). Statistical characteristics of energetic electron pitch angle distributions in the Van Allen probe era: 1. Butterfly distributions with flux peaks at preferred pitch angles. *Journal of Geophysical Research: Space Physics*, *127*(3), e2021JA029907. https://doi.org/10.1029/2021JA029907

Roederer, J. G. (1967). On the adiabatic motion of energetic particles in a model magnetosphere. *Journal of Geophysical Research*, *72*(3), 981–992. https://doi.org/10.1029/JZ072i003p00981

Roederer, J. G., & Schulz, M. (1969). Effect of shell splitting on radial diffusion in the magnetosphere. *Journal of Geophysical Research*, *74*(16), 4117–4122. https://doi.org/10.1029/JA074i016p04117

Roederer, J. G., & Schulz, M. (1971). Splitting of drift shells by the magnetospheric electric field. *Journal of Geophysical Research*, *76*(4), 1055–1059. https://doi.org/10.1029/JA076i004p01055

Russell, C. (1971). Geophysical coordinate transformations. *Cosmic Electrodynamics*, *2*, 184–196. Retrieved from http://sun.stanford.edu/~jsoc/keywords/Chris_Russel/http___www-ssc.igpp.ucla.edu_personnel_russell_papers_gct1.html_.pdf%20

Schulz, M., & Lanzerotti, L. J. (1974). Radial diffusion (pp. 81–113). https://doi.org/10.1007/978-3-642-65675-0_4

Selesnick, R. S., & Blake, J. B. (2002). Relativistic electron drift shell splitting. *Journal of Geophysical Research*, *107*(A9), SMP27-1–SMP27-10. https://doi.org/10.1029/2001JA009179

Shue, J., Chao, J. K., Fu, H. C., Russell, C. T., Song, P., Khurana, K. K., & Singer, H. J. (1997). A new functional form to study the solar wind control of the magnetopause size and shape. *Journal of Geophysical Research*, *102*(A5), 9497–9511. https://doi.org/10.1029/97JA00196

Shue, J., Song, P., Russell, C. T., Steinberg, J. T., Chao, J. K., Zastenker, G., et al. (1998). Magnetopause location under extreme solar wind conditions. *Journal of Geophysical Research*, *103*(A8), 17691–17700. https://doi.org/10.1029/98JA01103

Smirnov, A., Shprits, Y., Allison, H., Aseev, N., Drozdov, A., Kollmann, P., et al. (2022). Storm-time evolution of the equatorial electron pitch angle distributions in Earth's outer radiation belt. *Frontiers in Astronomy and Space Sciences*, *9*, 836811. https://doi.org/10.3389/fspas.2022.836811

Stasiewicz, K., Bellan, P., Chaston, C., Kletzing, C., Lysak, R., Maggs, J., et al. (2000). Small scale Alfvénic structure in the aurora. *Space Science Reviews*, *92*(3-4), 423–533. https://doi.org/10.1023/A:1005207202143

Turner, D. L., Kilpua, E. K. J., Hietala, H., Claudepierre, S. G., O'Brien, T. P., Fennell, J. F., et al. (2019). The response of Earth's electron radiation belts to geomagnetic storms: Statistics from the Van Allen probes era including effects from different storm drivers. *Journal of Geophysical Research: Space Physics*, *124*(2), 1013–1034. https://doi.org/10.1029/2018JA026066

Turner, D. L., Shprits, Y., Hartinger, M., & Angelopoulos, V. (2012). Explaining sudden losses of outer radiation belt electrons during geomagnetic storms. *Nature Physics*, *8*(3), 208–212. https://doi.org/10.1038/nphys2185

Usanova, M. E., Drozdov, A., Orlova, K., Mann, I. R., Shprits, Y., Robertson, M. T., et al. (2014). Effect of emic waves on relativistic and ultrarelativistic electron populations: Ground-based and Van Allen probes observations. *Geophysical Research Letters*, *41*(5), 1375–1381. https://doi.org/10.1002/2013GL059024

West, H. I. (1966). Some observations of the trapped electrons produced by the Russian high-altitude nuclear detonation of October 28, 1962. In B. M. McCormac (Ed.), *Radiation trapped in the Earth's magnetic field* (pp. 634–662). Springer.

West, H. I., Jr., Buck, R. M., & Walton, J. R. (1973). Electron pitch angle distributions throughout the magnetosphere as observed on OGO 5. *Journal of Geophysical Research*, *78*(7), 1064–1081. https://doi.org/10.1029/JA078i007p01064

Wygant, J. R., Bonnell, J. W., Goetz, K., Ergun, R. E., Mozer, F. S., Bale, S. D., et al. (2013). The electric field and waves instruments on the radiation belt storm probes mission. *Space Science Reviews*, *179*(1–4), 183–220. https://doi.org/10.1007/s11214-013-0013-7

Xiang, Z., Tu, W., Ni, B., Henderson, M. G., & Cao, X. (2018). A statistical survey of radiation belt dropouts observed by Van Allen probes. *Geophysical Research Letters*, *45*(16), 8035–8043. https://doi.org/10.1029/2018GL078907

Xiao, F., Yang, C., Su, Z., Zhou, Q., He, Z., He, Y., et al. (2015). Wave-driven butterfly distribution of Van Allen belt relativistic electrons. *Nature Communications*, *6*(1), 8590. https://doi.org/10.1038/ncomms9590

Xiong, Y., Chen, L., Xie, L., Fu, S., Xia, Z., & Pu, Z. (2017). Relativistic electron's butterfly pitch angle distribution modulated by localized background magnetic field perturbation driven by hot ring current ions. *Geophysical Research Letters*, *44*(10), 4393–4400. https://doi.org/10.1002/2017GL072558

Yu, Y., Fu, H. S., Wang, Z., Fu, W. D., & Cao, J. B. (2023). Formation of electron butterfly distribution by a contracting dipolarization front. *Geophysical Research Letters*, *50*(17), e2023GL104938. https://doi.org/10.1029/2023GL104938

Zhao, H., Friedel, R. H. W., Chen, Y., Reeves, G. D., Baker, D. N., Li, X., et al. (2018). An empirical model of radiation belt electron pitch angle distributions based on Van Allen probes measurements. *Journal of Geophysical Research: Space Physics*, *123*(5), 3493–3511. https://doi.org/10.1029/2018JA025277

Zhao, H., Li, X., Blake, J. B., Fennell, J. F., Claudepierre, S. G., Baker, D. N., et al. (2014a). Characteristics of pitch angle distributions of hundreds of keV electrons in the slot region and inner radiation belt. *Journal of Geophysical Research: Space Physics*, *119*(12), 9543–9557. https://doi.org/10.1002/2014JA020386

Zhao, H., Li, X., Blake, J. B., Fennell, J. F., Claudepierre, S. G., Baker, D. N., et al. (2014b). Peculiar pitch angle distribution of relativistic electrons in the inner radiation belt and slot region. *Geophysical Research Letters*, *41*(7), 2250–2257. https://doi.org/10.1002/2014GL059725